aerospace

MDPI

Article

An Experimental Investigation on Hypersonic Boundary Layer Stability over a Fin–Cone Configuration

Dailin Lv [1], Fu Zhang [2], Yifan Yang [1], Xueliang Li [1] and Jie Wu [1,*]

[1] Department of Engineering Mechanics, School of Aerospace Engineering, Huazhong University of Science and Technology, Wuhan 430074, China; d202580920@hust.edu.cn (Y.Y.); xueliang_li@163.com (X.L.)
[2] Beijing Aerospace Long March Vehicle Research Institute, Beijing 100076, China
* Correspondence: jiewu@hust.edu.cn

Abstract

To investigate the hypersonic boundary layer transition over complex three-dimensional configurations, this study conducted an experiment using infrared thermography, Rayleigh scattering visualization, and high-frequency pressure sensors in a Mach 6 Ludwieg wind tunnel. The infrared results indicate that increasing the Reynolds number promotes boundary layer transition on the model surface. Spectral analysis reveals a high-frequency peak centered at 250 kHz on the finless side of the windward surface. Comprehensive analysis indicates this represents high-frequency secondary instability triggered by the traveling crossflow mode in its nonlinear phase. On the finless side of the leeward surface, a typical Mack second-mode high-frequency instability amplification process is observed within the 140–280 kHz frequency band. Additionally, the spectrum results for the fin–cone junction became more complex. On the windward side, the primary energy concentration in the junction zone is observed between 80 and 200 kHz, with calculated wave packet velocities higher than those on the finless side. Wavelet analysis reveals that low-frequency modes are amplified first and gradually excite high-frequency components, with significant modal coupling appearing in the high-frequency region of the bicoherence. The leeward fin–cone junction exhibits dual-band characteristics at 60–120 kHz and 180–260 kHz, demonstrating stronger intermodal interactions. Both the windward and leeward surfaces of the fin show low-frequency transverse flow-like modes around 70–180 kHz. The spectral results for the windward and leeward sides are largely consistent, with only slight differences in amplitude levels and saturation positions.

Keywords: hypersonic boundary layer instability; transition; fin–cone configuration; wind tunnel experiment

Check for updates

Academic Editor: Kung-Ming Chung

Received: 14 January 2026
Revised: 2 February 2026
Accepted: 3 February 2026
Published: 6 February 2026

Copyright: © 2026 by the authors. Licensee MDPI, Basel, Switzerland. This article is an open access article distributed under the terms and conditions of the Creative Commons Attribution (CC BY) license.

1. Introduction

Hypersonic boundary layer transition remains a major source of uncertainty in the aerodynamic and aerothermodynamic design for hypersonic vehicles. Therefore, establishing a reliable understanding and predictive capability for hypersonic boundary layer transition based on underlying mechanisms is of paramount importance [1–3]. For canonical configurations, decades of research, including instability theories and high-fidelity wind-tunnel measurements, have established the onset conditions and downstream evolution of several key instability routes, such as the streamwise instability waves, crossflow instabilities, and attachment-line and Görtler instabilities. Practical hypersonic vehicles, however, employ fully three-dimensional geometries with embedded shock and expansion

features. In these flows, shock–boundary layer interaction, three-dimensional pressure gradients, and large-scale vortex systems can coexist within the same configuration, promoting the concurrent amplification of multiple instability mechanisms and strengthening nonlinear modal interactions [4–7]. Consistent with this trend, recent studies of complex lifting-body and blended-body configurations increasingly emphasize multi-mode behavior, vortex interference, and nonlinear evolution rather than a single dominant instability. For example, investigations associated with the X-33 program examined hypersonic boundary layer stability on Mach 6 and Mach 10 and indicated susceptibility to crossflow-related instabilities [8]. The X-51A forebody studies further demonstrated the sensitivity of roughness-induced transition to freestream noise. These studies also highlighted the requirement for quiet wind-tunnel testing in boundary layer state prediction and control [9,10]. Similarly, flight and wind-tunnel investigations of lifting-body platforms such as HIFiRE-5, BOLT, and HyTRV have shown that the dominant transition route can vary by region and operating condition, revealing the coupled effects of crossflow-related mechanisms, second-mode disturbances, and configuration-specific vortex systems [11–16].

For engineering-relevant blended configurations, extensive experimental and theoretical research has provided a strong foundation, yet key mechanistic questions remain. Gillerlain reported pressure, heat-transfer, and flow-visualization measurements at Mach 5 with an emphasis on separation and interference flow in the junction region [17]. Quiet-tunnel studies by Turbeville et al. used temperature-sensitive paint (TSP) and high-frequency pressure measurements on swept fin–cone configurations to research how sweep angle, leading-edge bluntness, and nose bluntness affect surface heating and spectral characteristics [18–21]. Numerical work by Knutson et al. combined direct numerical simulation (DNS) with linear parabolized stability equations to identify flow structures such as horseshoe vortices, leading-edge vortices, and crossflow [22,23].

Turbeville later extended these efforts to subscale BOLT and swept fin–cone configurations, utilizing infrared (IR) thermography and a rotatable measurement platform to document second-mode activity over the cone (175–300 kHz) and lower-frequency disturbances near the fin (50–170 kHz) [24,25]. On the theoretical side, McMillan applied a non-orthogonal spatial BiGlobal approach to a Mach 6 swept-fin–cone configuration to identify surface instability modes [26]. Riha et al. generalized spatial BiGlobal analysis to non-orthogonal coordinate systems suitable for complex geometries [27]. Middlebrooks et al. utilized TSP and wavelet analysis to extract crossflow streak signatures and demonstrated passive control via discrete roughness element arrays [28–30]. Peck investigated swept-fin boundary layers using the harmonic linearized Navier–Stokes method, revealing a strong wavelength dependence of crossflow-related disturbances [31,32]. At high Reynolds and Mach numbers, Meng et al. examined a flared-cone–swept-fin configuration and showed that SBLI coupled with adverse pressure gradients can generate triangular high-temperature-rise regions [33,34]. Meanwhile, Li et al. used high-fidelity optical diagnostics, such as focused laser differential interferometry (FLDI), to obtain high-resolution measurements of microscopic instability-wave signatures on blended configurations [35]. Overall, among these configurations, complex three-dimensional geometries and variations in angle of attack can strongly enhance interactions between multiple instability modes and the surrounding vortex system. The transition process consequently exhibits more pronounced regional differences and stronger nonlinear interactions. For blended-fin–body configurations in this study, several three-dimensional effects can coexist on the same vehicle, including junction flows, leading-edge vortices, and corner expansion. This makes such configurations a valuable test case for studying multi-modal interactions and region-dependent transition behavior.

These efforts have advanced the understanding of hypersonic transition on complex configurations. However, hypersonic boundary layer instability and transition upon blended fin–body remain outstanding. This work highlights the engineering significance of asymmetric fin–cone configurations and junction effects, specifically targeting the current void in unified-condition measurements. Existing data often fails to provide the high temporal bandwidth and spatial resolution required across multiple regions simultaneously. Consequently, region-specific transition prediction models and control strategies require further development and validation using more comprehensive experimental datasets. To this end, the present study investigates an asymmetric swept-fin–cone configuration in the Φ 0.5 m Mach 6 Ludwieg-tube wind tunnel at Huazhong University of Science and Technology. High-frequency surface pressure measurements are combined with IR thermography and the Rayleigh scattering technique to quantify transition and aerothermal responses across a range of Reynolds numbers. Power spectral density (PSD), cross-correlation, and wavelet analyses are used to identify key instability modes and track how they interact and evolve across different regions.

2. Experimental Facility and Data Processing Methods

2.1. Model and Pressure Sensor Setup

The experimental model features a blended configuration with a single-sided swept fin. The main body of the model is constructed of Polyether ether ketone (PEEK), while the nose, base, and central tie rod are fabricated from stainless steel. The model was asymmetrically modified in both body geometry and fin arrangement. The upper half of the cone was defined as the leeward side, with a forebody half-cone angle of 7.30°. An inward corner was introduced on this side at x = 202.2 mm, which reduced the local half-cone angle to 4.0° and generated a pronounced expansion wave. The lower half of the cone was defined as the windward side, featuring a body half-cone angle of 2.7°. The coordinate origin is located at the nose apex, and the x-axis is defined along the streamwise direction. The fin-root leading-edge location was set at x = 102.5 mm, which is approximately 87.8 mm upstream of the leeward expansion corner. This placement was selected to emphasize the influence of the expansion corner on boundary layer evolution in the fin–cone junction. The scaled model has a total length of 464.125 mm and includes a nose section with a blunt radius of Rn = 1.125 mm. To obtain detailed pressure distributions over the windward and leeward finless sides (R1 and R2), the fin–cone junction regions (R3 and R4), and the fin surface regions (R5 and R6), three pressure-tap arrays were installed on the model surface. In the windward fin–cone junction region (R3), pressure taps No. 1–No. 6 were arranged streamwise over x = 296–446 mm with a spacing of 30 mm. The pressure taps were offset by a constant distance of 10 mm from the fin edge, while the corresponding reference taps were placed on the windward finless side (R1) to provide baseline measurements. In the leeward fin–cone junction region (R4), the primary taps No. 1–No. 8 were arranged streamwise over x = 288–428 mm with a spacing of 20 mm, and symmetric reference taps were installed on the leeward finless side (R2). For the fin surface regions (R5 and R6), through-hole pressure taps No. 1–No. 7 were arranged along a direction approximately parallel to the fin root over x = 261–441 mm with a spacing of 30 mm. An additional tap (No. 8) was placed 15 mm outboard from tap No. 5 along the local surface-normal direction. With this geometric design and instrumentation layout, pressure distributions on the finless reference side, the fin–cone junction, and the fin surfaces can be captured comprehensively with high spatial resolution. The resulting dataset provides a reliable basis for subsequent boundary layer stability analyses and transition-mechanism investigations. The detailed layout is shown in Figures 1–4.

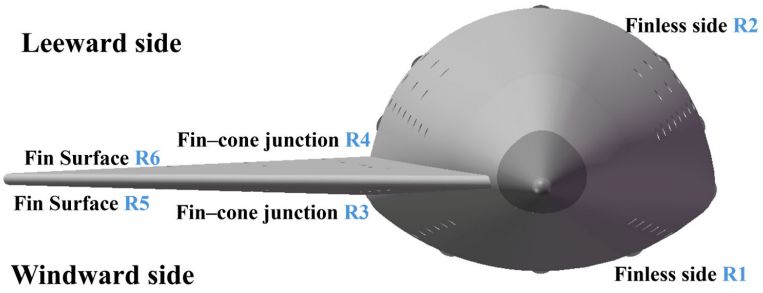


Figure 1. Schematic of the model surface partitioning. The six regions of interest are defined as the windward finless side (R1), the leeward finless side (R2), the windward fin–cone junction (R3), the leeward fin–cone junction (R4), the windward fin surface (R5), and the leeward fin surface (R6).

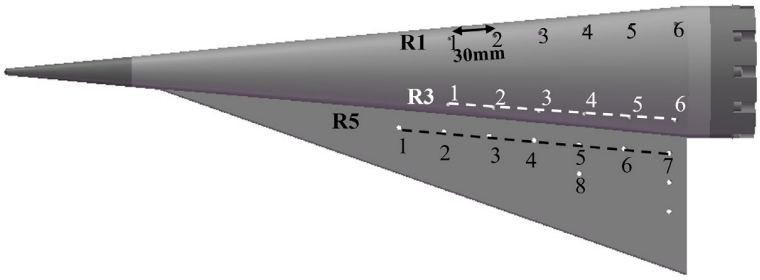


Figure 2. Layout of the surface-pressure sensors on the windward surface of the model.

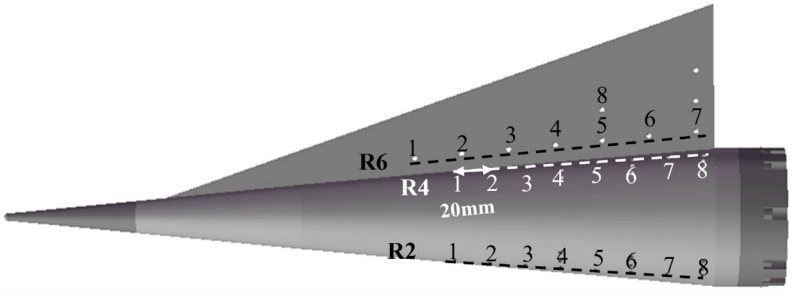


Figure 3. Layout of the surface-pressure sensors on the leeward surface of the model.

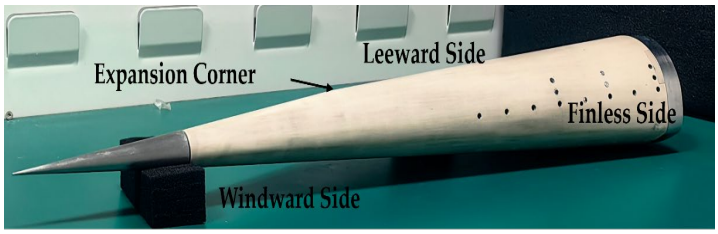


Figure 4. Photograph of the asymmetric blended fin–cone model with a single swept fin.

2.2. Experimental Facility and Experimental Case

The experiments were carried out in the Φ 0.5 m Mach 6 Ludwieg-tube wind tunnel at Huazhong University of Science and Technology. The facility comprises six primary components, i.e., the storage tube, a fast-acting valve, a Laval nozzle, a test section, an expansion section, and the vacuum tank. It offers broad operating flexibility, with a total-pressure range of 0.5–3 MPa and total temperature up to 600 K. The maximum unit Reynolds number of the freestream can reach the order of 3.2×10^7 m^{-1}, with an efficient runtime at 100 ms. The normalized Pitot total-pressure fluctuation level is stably maintained within 0.7–1.5%, ensuring a reliable disturbance environment for the study of transition [36]. The wind tunnel has been verified to possess excellent repeatability [37],

thereby guaranteeing the reliability of the experimental data. These capabilities make the wind tunnel particularly capable for experimental investigations into hypersonic boundary layer transition.The experimental conditions are summarized in Table 1.

Table 1. Experimental case.

Ma	P_0 (Bar)	T_0 (K)	Re (1/m)
6	6.00	420.60	6.72×10^6
6	7.00	420.60	7.85×10^6
6	9.00	420.60	1.01×10^7

2.3. Infrared Camera

The infrared thermography was performed using a high-precision infrared camera. The system provides a thermal sensitivity of 15 mK, which is sufficient to resolve subtle thermal signatures on the surface temperature-rise field. The camera was operated at a full-frame acquisition rate of 50 Hz, matching the effective run time of the Ludwieg-tube facility. The camera viewing range has a format of 512 × 620 pixels, and the field of view was adjusted to cover the critical regions of the model surface. The key region extends from approximately 30 mm upstream of the expansion corner to the aft end of the model. Data acquisition was synchronized with the wind-tunnel startup button. At the onset of the useful test time duration, the IR system was triggered to record the surface-temperature evolution over a 100 ms acquisition window. During post-processing, a dynamic reference correction was applied to enhance the signal-to-noise ratio. A reference temperature field, T_0, was obtained by averaging frames from a 100 ms window before the tunnel start-up process. Similarly, an experimental temperature field, T1, was extracted from a 100 ms window during the quasi-steady test period. The temperature-rise field was then computed as the above temperatures' difference. This procedure effectively reduces background drift and enables robust identification and accurate localization of the boundary layer transition front.

2.4. Pressure Sensor Postprocessing

High-frequency PCB-132B38 piezoelectric pressure transducers (PCB Piezotronics (Depew, NY, USA)) were employed to measure surface-pressure fluctuations. Each sensor has a 3.18 mm diameter sensing diaphragm, a pressure resolution of approximately 7 Pa, and an intrinsic resonance frequency exceeding 1 MHz. The sensor bandwidth ranges from 11 kHz to 1 MHz, enabling the measurement of high-frequency instability-wave content. The transducers were connected to PCB 482C05 constant-current signal conditioners through PCB 003C10 low-noise coaxial cables, and the conditioned signals were digitized by the data acquisition system at 3 MHz with 16-bit vertical resolution. The pressure time series were transformed into the frequency domain to compute the power spectral density, which is expressed as follows:

$$\mathrm{S}(f) = \lim_{\mathrm{T}\to\infty} \frac{1}{\mathrm{T}} \int_{-\frac{1}{2\mathrm{T}}}^{\frac{1}{2\mathrm{T}}} \mathrm{s(t)e^{-i2\pi ft}dt} \tag{1}$$

$$PSD(f) = \lim_{t\to\infty} \frac{1}{t} E[X(f)X^*(f)] \tag{2}$$

where PSD(f) is the spectral density at frequency f, E [] denotes expectation, X(f) is the Fourier transform of the time series, and X*(f) its complex conjugate. In addition, cross-correlation analysis of the PCB pressure signals measured at adjacent locations is employed

to determine the propagation time delay of the instability waves, from which their convective velocities can be estimated. Together with wavelet analysis, which provides a time–frequency decomposition of the signals at each measurement point, this approach allows the evolution and local development of the instability waves at different spatial locations to be characterized in detail.

The pressure signals were sampled at F_s = 3 MHz and converted to pressure using channel-specific calibration factors. For spectral analyses, the signals were band-pass filtered using Butterworth filters to remove low-frequency drift and high-frequency noise. PSDs were computed using Welch's method with a Hamming window of length nfft = 1024 and 50% overlap, yielding a frequency resolution $\Delta f = F_s/\text{nfft} \approx 2.93$ kHz. Convection velocity was estimated from the lag at the peak of the normalized cross-correlation between adjacent sensors, $U_c = \Delta x/\Delta t$. Time-frequency characteristics were obtained by continuous wavelet transforms (cwt) using the Morse wavelet with Fs = 3 MHz. Nonlinear coupling was quantified by normalized bicoherence computed with nfft = 2×10^{11}, a Hamming window of length nsamp = 4096, and 50% overlap, and interpreted based on coherent regions of elevated bicoherence in the $f_1 - f_2$ plane.

2.5. Rayleigh Scattering

A 200 mJ Nd:YAG dual-pulse laser was employed to generate a laser sheet with an approximate thickness of 500 μm to illuminate the measurement region. The laser operated at a wavelength of 532 nm with a pulse width of 0.6 ns. The inter-pulse delay was set to 0.6 μs, and the dual-pulse repetition rate was 18 Hz. The CMOS camera exposure was synchronized using a timing controller to ensure that paired images were acquired during each wind-tunnel run. The camera field of view was 140.26×98.46 mm^2 with a resolution of 4096×3096 pixels. This arrangement provides high spatiotemporal resolution and a high signal-to-noise ratio, enabling detailed characterization of particle-seeded flow structures using tracer particles with diameters below 50 nm. Under the present optical configuration, the measured intensity is dominated by particle scattering rather than molecular Rayleigh scattering from the gas. For clarity, the revised manuscript refers to this method as seeded particle-scattering visualization. The seeding level was kept low and was used only to enhance image contrast. It is not expected to modify the mean boundary layer state or the transition process. Figure 5 illustrates the Rayleigh scattering system layout and its integration with the wind-tunnel facility.

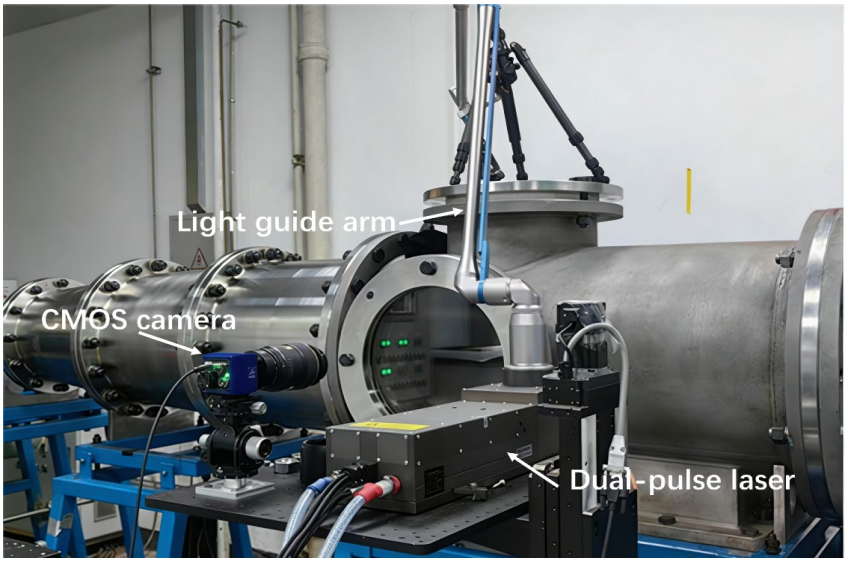
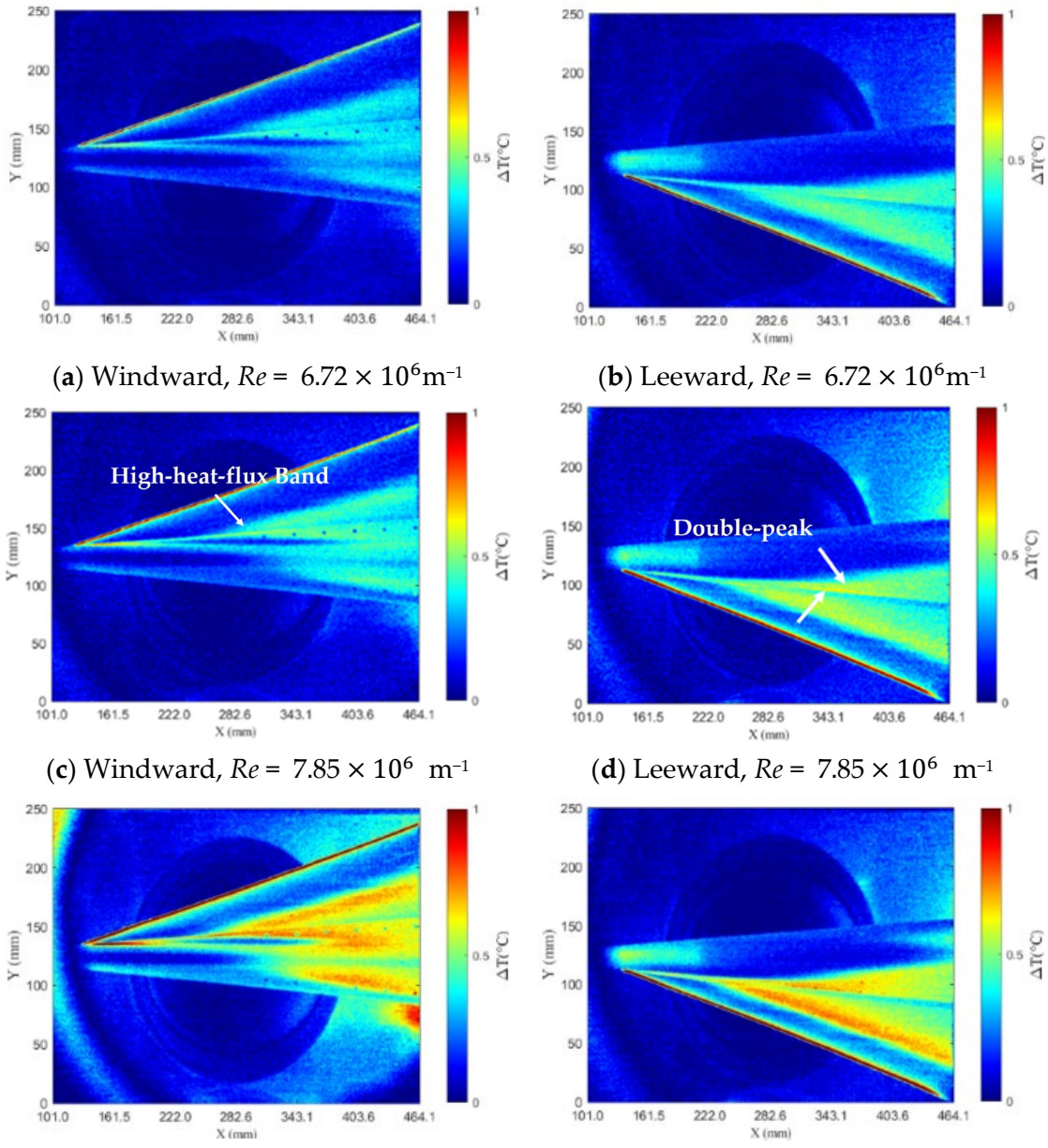


Figure 5. Schematic of the Rayleigh scattering measurement setup.

3. Experimental Results and Analysis

3.1. Infrared Result Analysis

Figure 6 shows representative infrared temperature-rise fields on the windward and leeward surfaces from Reynolds numbers of 6.72×10^6/m to 1.01×10^7/m. As the Reynolds number increases, the transition fronts on both surfaces move upstream generally. On the windward finless side, the temperature-rise pattern resembles that of a classical elliptic cone [38]. A long laminar region is present downstream of the nose. Farther downstream, streaky heating bands appear and then expand into broader high-temperature-rise zones, corresponding to the boundary layer transition from laminar to turbulent flow. On the leeward surface, the transition front is usually farther downstream than on the windward side. This delay is associated with the expansion corner and three-dimensional geometry [35].



(**a**) Windward, $Re = 6.72 \times 10^6 m^{-1}$ (**b**) Leeward, $Re = 6.72 \times 10^6 m^{-1}$

(**c**) Windward, $Re = 7.85 \times 10^6\ m^{-1}$ (**d**) Leeward, $Re = 7.85 \times 10^6\ m^{-1}$

(**e**) Windward, $Re = 1.01 \times 10^7\ m^{-1}$ (**f**) Leeward, $Re = 1.01 \times 10^7\ m^{-1}$

Figure 6. Infrared results on the windward side at different Reynolds numbers.

In the fin–cone junction region, a high-heat-flux band appears on the windward side, oriented nearly parallel to the junction line. As the Reynolds number increases, this band

shifts upstream and gradually widens, with its downstream end merging continuously with the transition streaks on the fin surface. This indicates that this region serves as a critical junction for the interactions between three-dimensional vortex systems and boundary layer instabilities. Region R4 exhibits a characteristic 'double-peak' heat-flux distribution: one high-heat-flux band is located near the junction line, while a secondary high-heating zone exists further outboard. These two peaks are separated by a relatively weak "valley" region, suggesting the coexistence of instability waves across multiple frequency bands and intense three-dimensional vortex structures [29].

Infrared results for the fin surface regions indicate that the transition fronts in regions R5 and R6 are oriented nearly parallel to the swept leading edge. The flow remains laminar upstream of the transition front, characterized by low and smooth surface temperature-rise, followed by the appearance of regular streamwise streaks that eventually evolve into a high-heat-flux band further downstream. Consistent frequencies on both sides of the surface indicate that traveling crossflow modes are the primary cause of instability in both regions. However, the morphology and evolution of the infrared streaks in regions R5 and R6 exhibit certain differences. The transition onset in region R5 occurs slightly earlier than that on the leeward side across most of the span. Downstream of these streaks, "sawtooth-like" secondary heating structures are observed. This spatial pattern is highly consistent with the typical infrared signatures of the nonlinear development and secondary instability of crossflow modes.

3.2. Rayleigh Scattering Results

To confirm the dominant instability on the windward finless side, Rayleigh scattering visualization was applied to observe the boundary layer along the windward body centerline. This technique provides high spatial resolution for identifying small-scale structures. Figure 7 presents representative instantaneous Rayleigh scattering images. Coherent wave packet structures emerge within the boundary layer and convect downstream. These packets are spatially periodic and remain highly coherent over a finite streamwise distance. Their form is consistent with flow structures typically observed during the secondary instability stage of traveling crossflow disturbances [39].

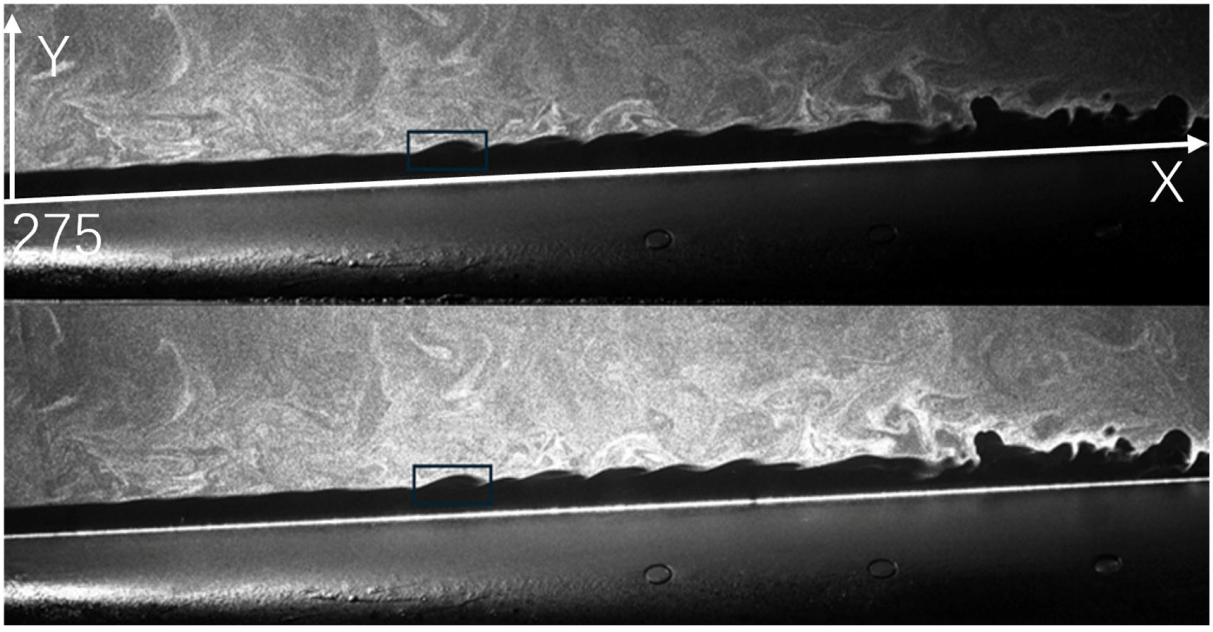


Figure 7. Representative instantaneous Rayleigh scattering images near the windward body centerline under a typical condition.

To quantify the propagation, individual wave packets were tracked across consecutive frames. The measured displacement and frame separation time yield a convection velocity of approximately $0.78U_e$. This value agrees with reported phase speeds for traveling crossflow disturbances in the secondary instability stage. Farther downstream, the wave packets grow in amplitude, then approach saturation, and finally break down. These observations support the view that the high-frequency spectral peak on the windward finless side is produced by the secondary instability of a traveling crossflow mode in the nonlinear stage.

Figure 8 shows the Rayleigh scattering results near the leeward body centerline. The leeward surface features a geometric corner that produces an expansion wave. This expansion reduces the boundary layer thickness compared to that on the windward side. Consequently, tracer particles struggle to penetrate the boundary layer, leading to reduced image contrast. Only indistinct bright and dark patterns are visible over a short streamwise range. Their spatial scale is similar to the windward patterns, but obvious growth is not identified further downstream. Therefore, the observed instability mode on the leeward side cannot be determined solely by Rayleigh scattering. Identification of the leeward mode relies on the subsequent analysis of high-frequency pressure spectra and cross-correlation results.

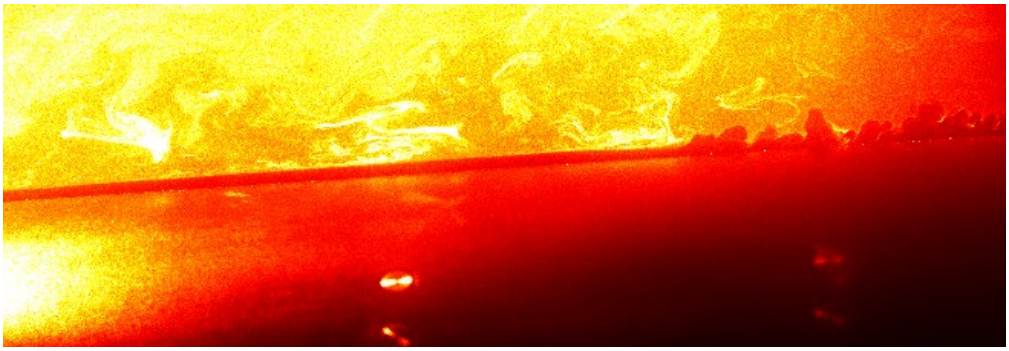


Figure 8. Representative instantaneous Rayleigh scattering images near the leeward body centerline under a typical condition.

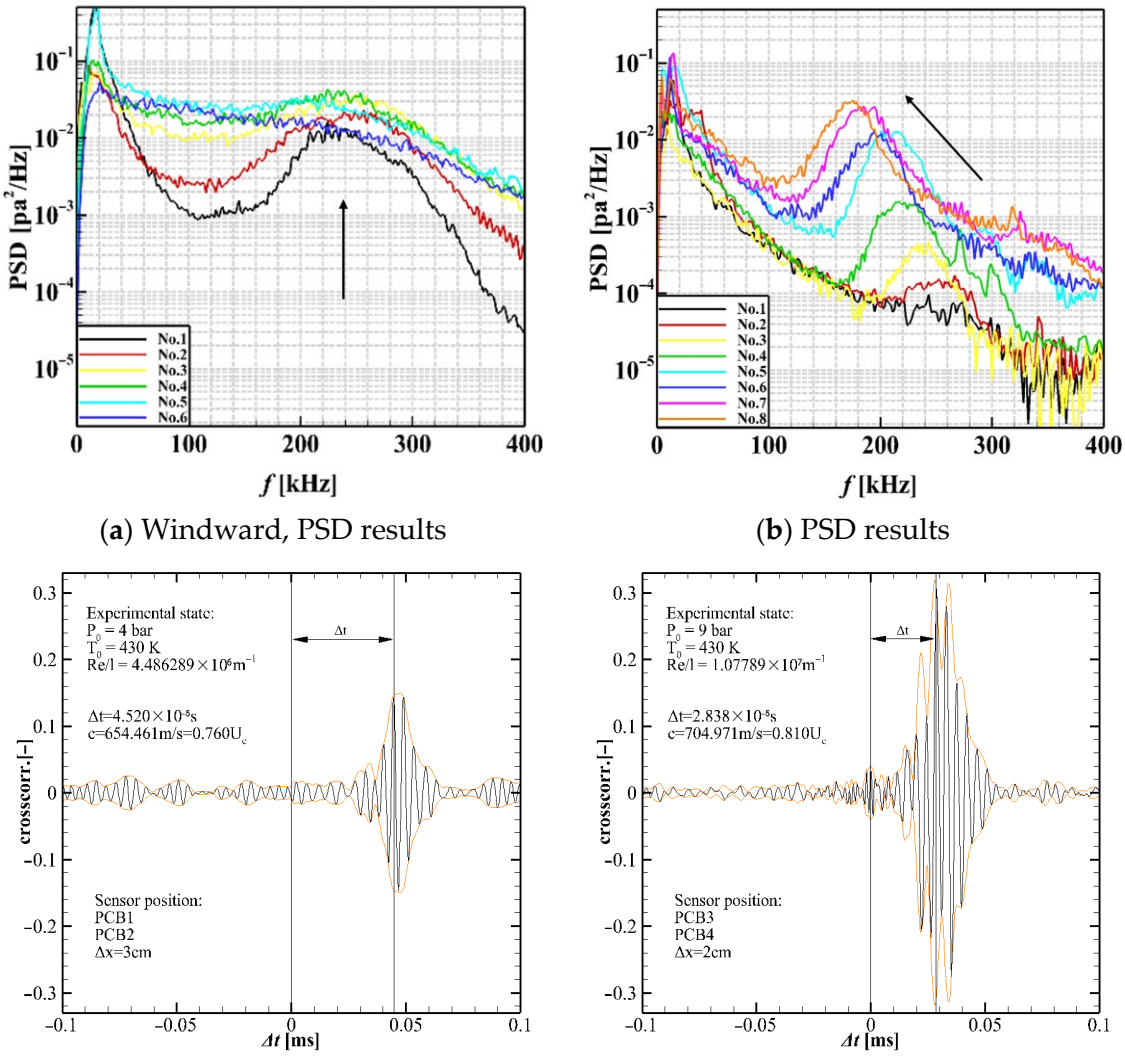
3.3. Analysis of Pulsation Spectrum

3.3.1. Pressure Fluctuation Spectral Analysis on the Finless Side

Pressure fluctuation spectra for the finless sides are summarized in Figure 9. In Region R1, at $Re = 1.01 \times 10^7$ m^{-1}, the PSD shows a clear, narrow wave peak frequency of approximately 250 kHz. The corresponding amplitude of pressure fluctuation amplifies as the flow develops along the streamwise direction, and it reaches the maximum near Station No. 6. The arrows indicate the streamwise development direction of the unstable-wave signatures. Cross-correlation yields a convection velocity of approximately $0.76U_e$, which is lower than that of Mack waves. Combined with the wave packet structures observed in Rayleigh scattering, this high-frequency peak is attributed to the secondary instability of traveling crossflow disturbances. The sustained growth indicates that it is a primary driver of transition in Region R1.

Figure 10 provides continuous wavelet spectra at four streamwise stations along the streamline in Region R1. A concentrated high-frequency wave appears between 150 and 350 kHz. The arrows mark the high-energy-density streaks in the time–frequency plane, which correspond to the wave-packet signatures of the dominant mode.This mode is visible at the most upstream Station No. 1, though the energy is weak. Moving downstream, these streaks become more frequent and intense, indicating pronounced amplification. At Station

No. 4, the spectral wave broadens with evident local modulation, indicating the occurrence of nonlinear growth and the incipient onset of breakdown.



(**a**) Windward, PSD results (**b**) PSD results

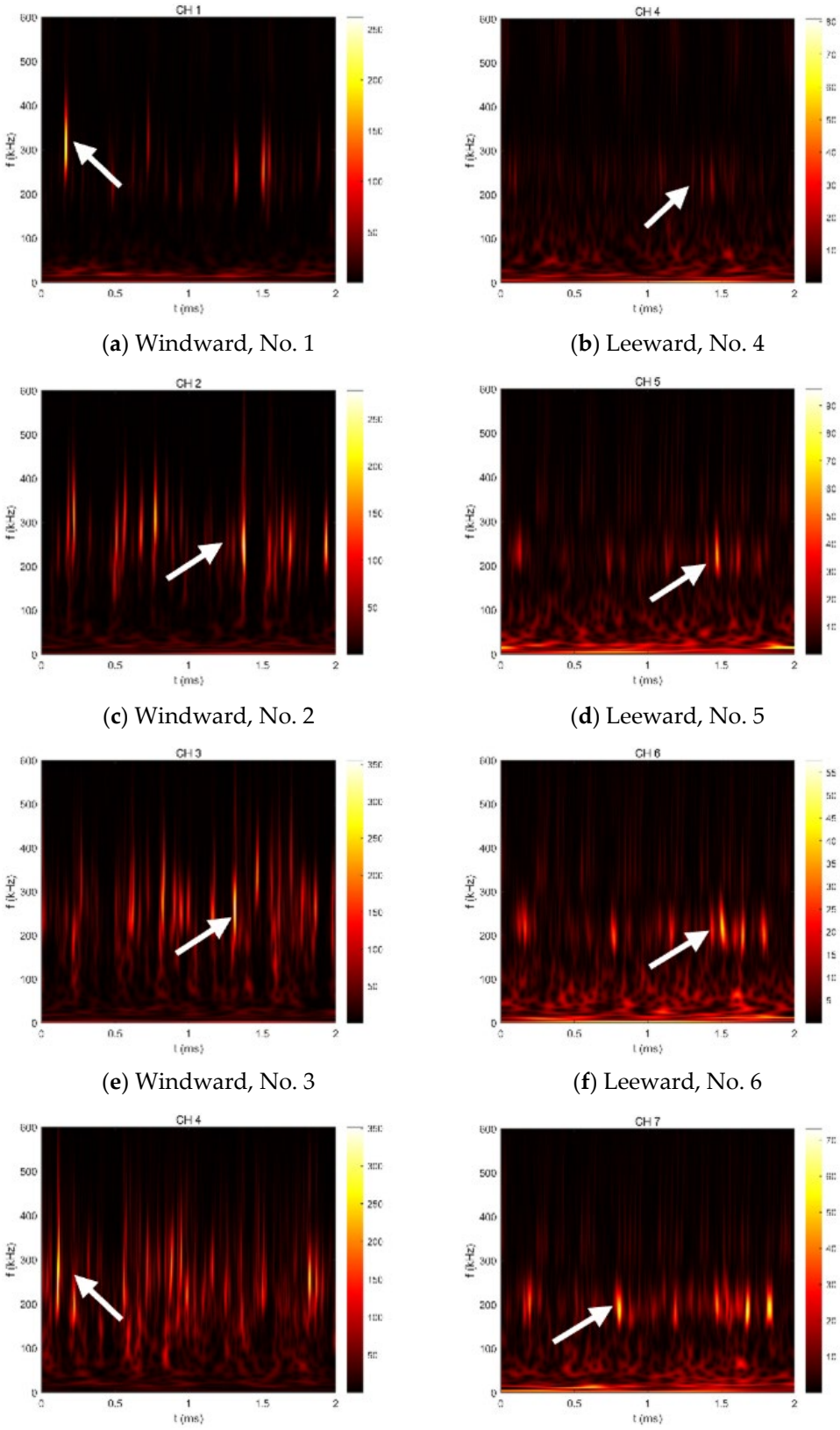
(**c**) Windward, cross-correlation results (**d**) Leeward, Cross-correlation results

Figure 9. Power spectral density spectra and multi-sensor cross-correlation results of surface-pressure fluctuations in the finless-side regions R1 and R2.

In Region R2, the PSD reveals a high-frequency instability in the 140–280 kHz range. At the most upstream Station No. 1, the spectrum is smooth and broadband, consistent with a laminar boundary layer. From Station No. 2 onward, a distinct peak emerges. The peak amplitude increases downstream, reaches saturation at mid-stream stations, and decreases slightly farther downstream. The peak frequency also shifts slightly lower with streamwise distance, consistent with boundary layer thickening. Cross-correlation yields a convection velocity of about $0.81U_e$. Therefore, based on the frequency range and propagation speed, this component is classified as a second-mode instability.

The wavelet spectra in Figure 10 show a similar trend for Region R2. A distinct energy wave is concentrated between 140 and 280 kHz, appearing as intermittent, wave packet-like streaks in the time domain. Relative to the low-frequency broadband background, this wave exhibits stronger localization in the time-frequency plane, indicating that a dominant instability mode governs the disturbances in Region R2. From Station No. 4 to No. 7, the events become much more frequent and stronger. At Station No. 7, the wave shows spectral broadening and increased intermittency. Therefore, together with the PSD and

cross-correlation results, this behavior matches the typical time–frequency evolution of second-mode instability during its later stage modulation.



(**a**) Windward, No. 1 (**b**) Leeward, No. 4

(**c**) Windward, No. 2 (**d**) Leeward, No. 5

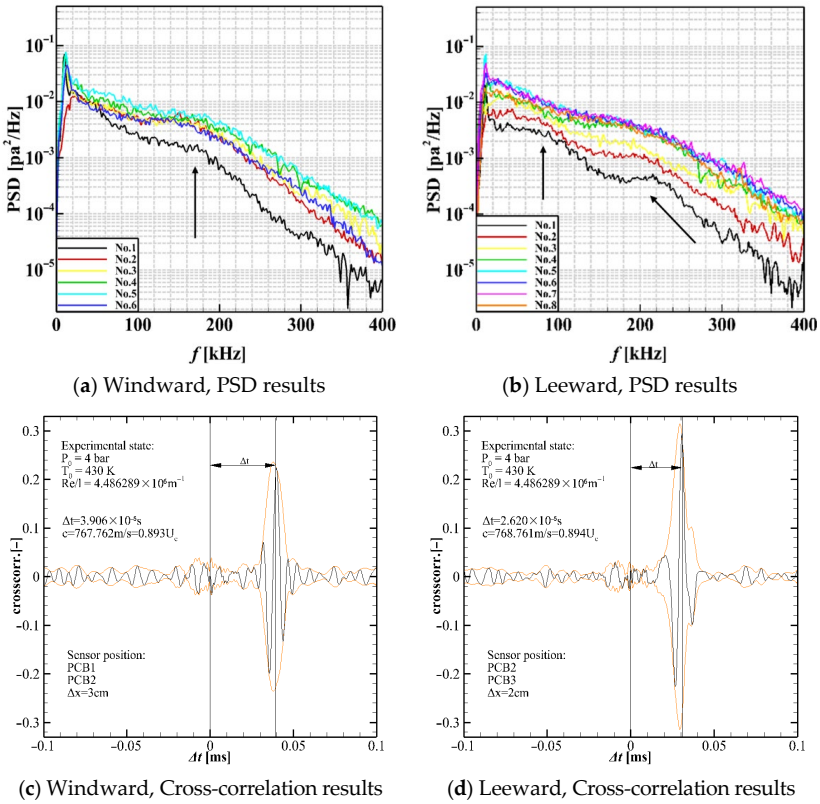
(**e**) Windward, No. 3 (**f**) Leeward, No. 6

(**g**) Windward, No. 4 (**h**) Leeward, No. 7

Figure 10. Wavelet spectra of the surface-pressure signals at selected streamwise stations along the same streamline in the finless-side regions R1 and R2.

3.3.2. Pressure Fluctuation Spectral Analysis on the Fin–Cone Junction

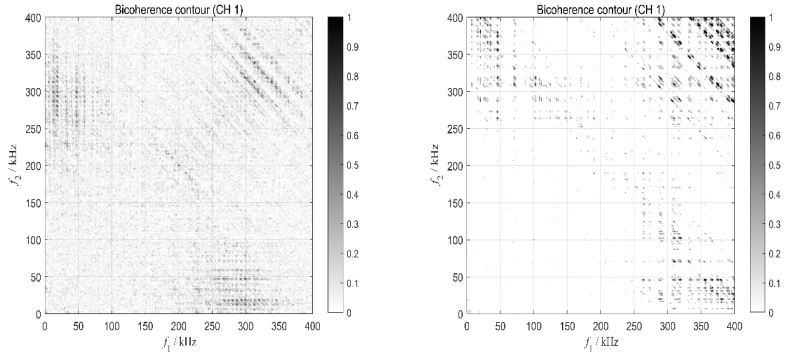
Figure 11 summarizes the pressure fluctuation behavior at the fin–cone junction on the windward and leeward sides. Several instability components exist in this region and overlap in frequency. Figure 12 presents the corresponding bispectral results to help identify nonlinear interactions.



(**a**) Windward, PSD results (**b**) Leeward, PSD results

(**c**) Windward, Cross-correlation results (**d**) Leeward, Cross-correlation results

Figure 11. Power spectral density spectra, multi-sensor cross-correlation results, and bispectral analysis of surface-pressure fluctuations in the fin–cone junction regions R3 and R4.

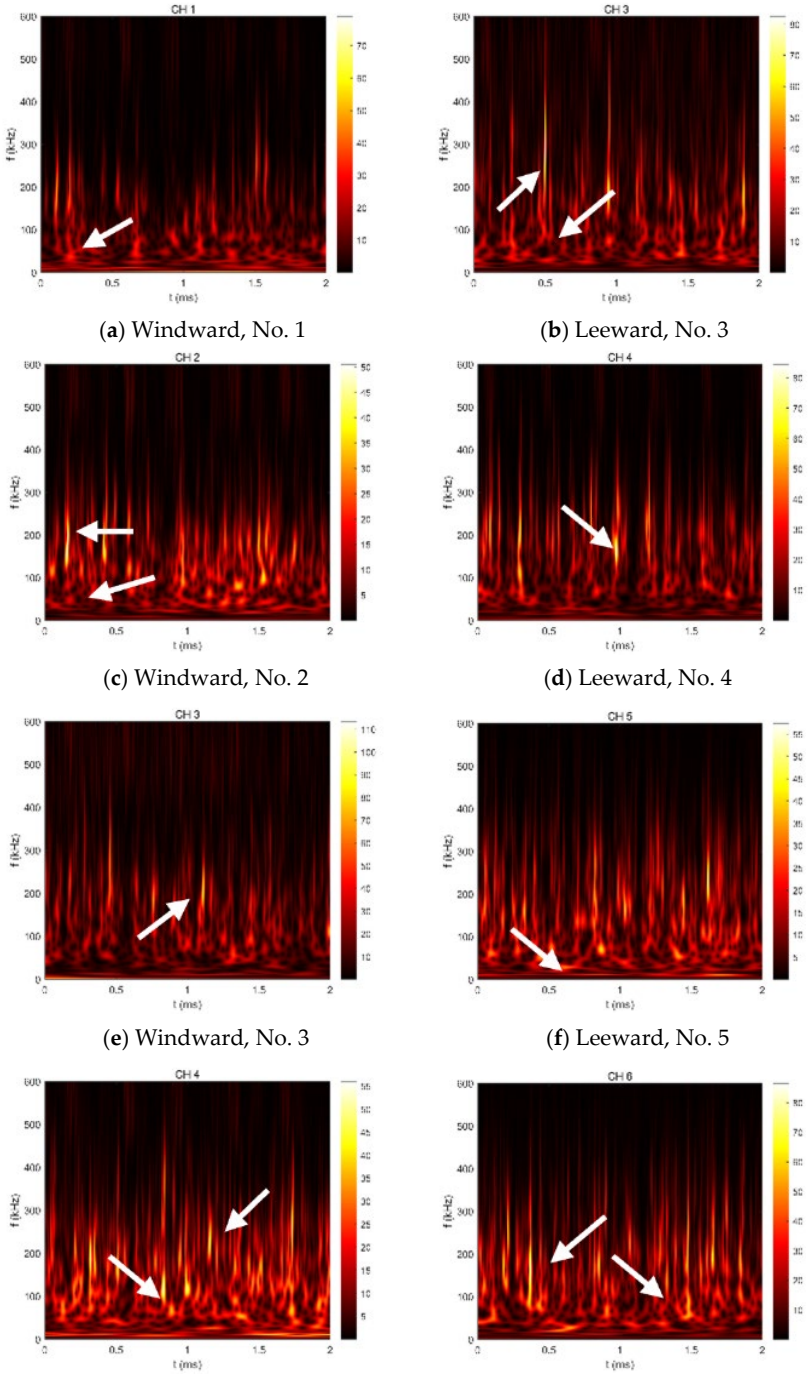


(**a**) Windward, No. 1 (**b**) Leeward, No. 3

Figure 12. Normalized bicoherence spectra of the surface-pressure signals in the fin–cone junction regions.

In Region R3 on the windward junction, the PSD shows a peak wave in 80–200 kHz. As the flow moves downstream, the peak frequency shifts slightly upward and the energy broadens. Cross-correlation indicates that disturbances convect at approximately $0.89U_e$. This value is significantly higher than the convection speed on the finless side and is closer to the edge velocity. The time–frequency characteristic at the junction is different from that in Region R1. In Region R1, the wavelet spectra are dominated by a 150–350 kHz mode

with intermittent wave packets. At the fin–cone junction, Figure 13 shows multiple modes occurring simultaneously. At Station No. 1, a lower frequency component (80–200 kHz) appears first and amplifies downstream. Beginning at Station No. 2, higher-frequency content becomes more pronounced. At Stations No. 3 and No. 4, both branches carry strong energy and exhibit wave packet behavior with clear temporal modulation. This trend suggests that a low-frequency primary mode amplifies first, followed by nonlinear effects that promote higher-frequency content. The process above results in stronger interactions and energy transfer within the three-dimensional junction flow.



(**a**) Windward, No. 1 (**b**) Leeward, No. 3

(**c**) Windward, No. 2 (**d**) Leeward, No. 4

(**e**) Windward, No. 3 (**f**) Leeward, No. 5

(**g**) Windward, No. 4 (**h**) Leeward, No. 6

Figure 13. Wavelet spectra of the surface-pressure signals at selected streamwise stations along the same streamline in the fin–cone junction regions R3 and R4.

Figure 12 quantifies these interactions at station No. 1. Normalized bicoherence is predominantly elevated in the high-frequency region where f_1 and f_2 exceed 200 kHz. The presence of multiple diagonal banded features indicates three-wave interactions and harmonic generation inside the second-mode wave. It also implies clear quadratic phase interactions among the high-frequency components. In contrast, the bicoherence for low–low pairs is close to zero, and most low–high pairs remain weak. This behavior suggests that low-frequency disturbances affect the high-frequency wave mainly through amplitude modulation rather than strong phase interactions. Overall, the bispectral results indicate a pronounced nonlinear stage and energy redistribution at this station.

In Region R4 on the leeward junction, the PSD shows two separate waves at 60–120 kHz and 180–260 kHz. Cross-correlation yields a convection velocity close to $0.89U_e$. The 180–260 kHz component cannot be interpreted as a simple second harmonic of the higher frequency wave. While the 180–260 kHz wave is mainly associated with second-mode instability, the 60–120 kHz wave is instead related to three-dimensional vortex motion and large-scale shear structures. This lower-frequency band likely stems from the low-frequency unsteadiness and large-scale motion of the junction vortex system, potentially representing unsteady behavior induced by the horseshoe vortex. These structures are further enhanced by the presence of the expansion corner.

Wavelet spectra at the leeward junction show a complex bi-modal process. Farther downstream, both branches become energetic and show wave packet behavior. High-frequency packets often appear near the amplitude maxima of the low-frequency component. This consistency indicates strong nonlinear interactions and energy transfer from large-scale disturbances to small-scale instability waves. In Region R4, the bicoherence level is higher overall, with a broad continuous region where $f_1, f_2 > 250$ kHz. This feature implies intense wave interactions inside the second-mode wave. Strong responses also occur in the low–high region, indicating enhanced interactions between low-frequency large-scale motion and the high-frequency second mode. Together, these results indicate a nonlinear stage in Region R4, where both high–high and low–high interactions are critical.

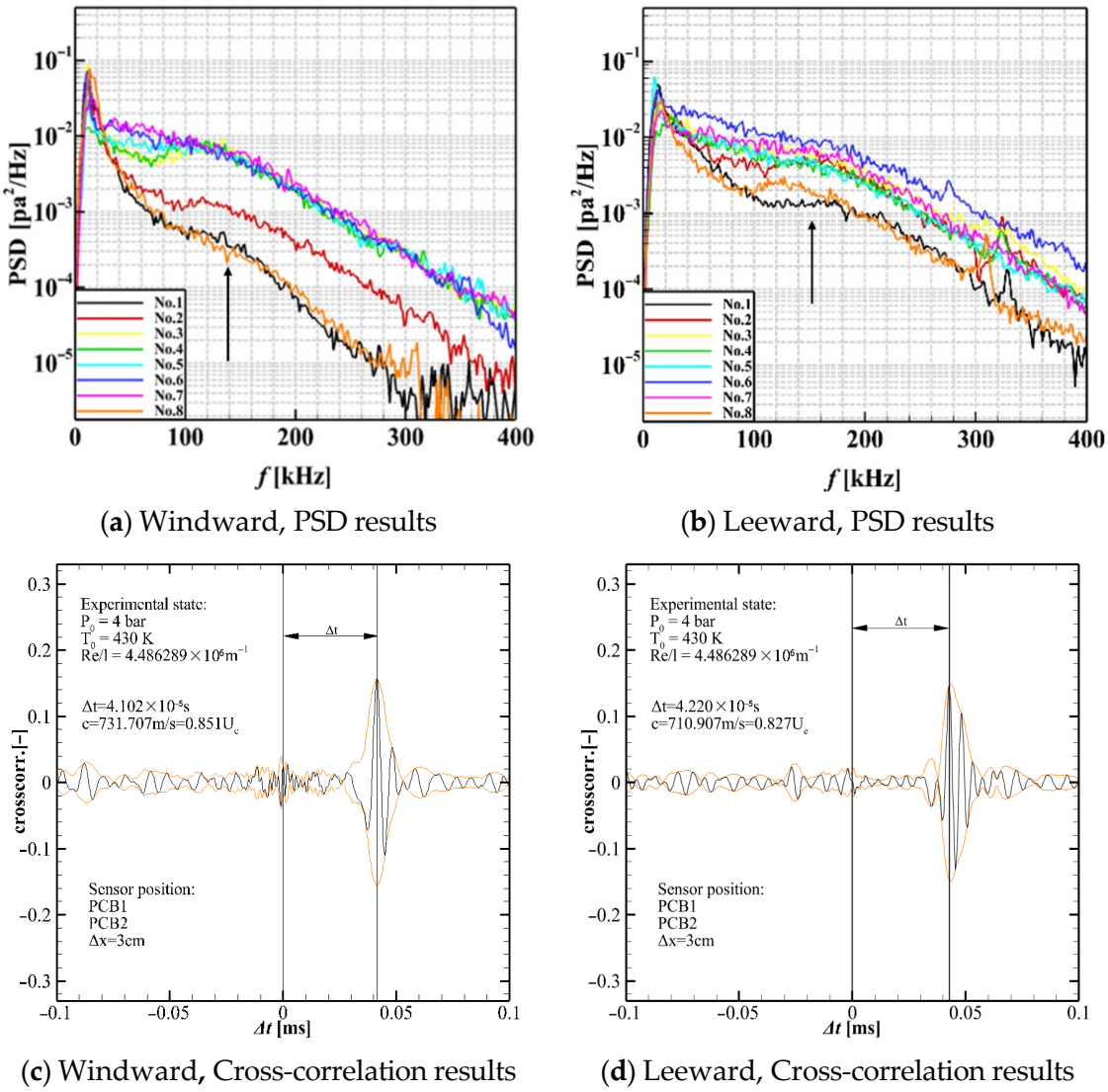
3.3.3. Pressure Fluctuation Spectral Analysis on the Fin Surface

Pressure spectra for the fin surface region R5 and R6 are shown in Figure 14. The PSD results in Region R5 show a relatively concentrated high-frequency wave within the range highlighted in Figure 15. The wave amplifies in amplitude over the initial stations and then decreases gradually farther downstream. In the fully turbulent region, the spectrum becomes broadband with energy spreading over a much wider frequency range in a continuous distribution.

Figure 15 presents the continuous wavelet spectra of the pressure signals at several streamwise locations along the same streamline in regions R5 and R6. At Stations No. 2 and No. 4, this frequency wave becomes more pronounced and intense, indicating sustained downstream amplification. At Station No. 8, the low-frequency wave weakens again. Some higher-frequency content is visible as faint vertical streaks, but its energy remains much lower than the low-frequency branch. These results indicate that fluctuations in Region R5 are mainly governed by a low-frequency, crossflow-type mode. Its downstream growth is consistent with the transition front movement inferred from the infrared streak patterns.

In Region R6, an unstable wave is observed in a similar frequency range, with a representative frequency near 140 kHz. Relative to Region R5, the amplification starts slightly farther upstream, and the low-frequency energy is stronger. This behavior suggests additional modulation of the leeward-fin boundary layer, likely involving three-dimensional

effects. Compared with the fin–cone junction, the fin surface sensors are farther from the expansion corner and the horseshoe-vortex core. Therefore, crossflow modes and their secondary instabilities have a more direct influence on the transition process.

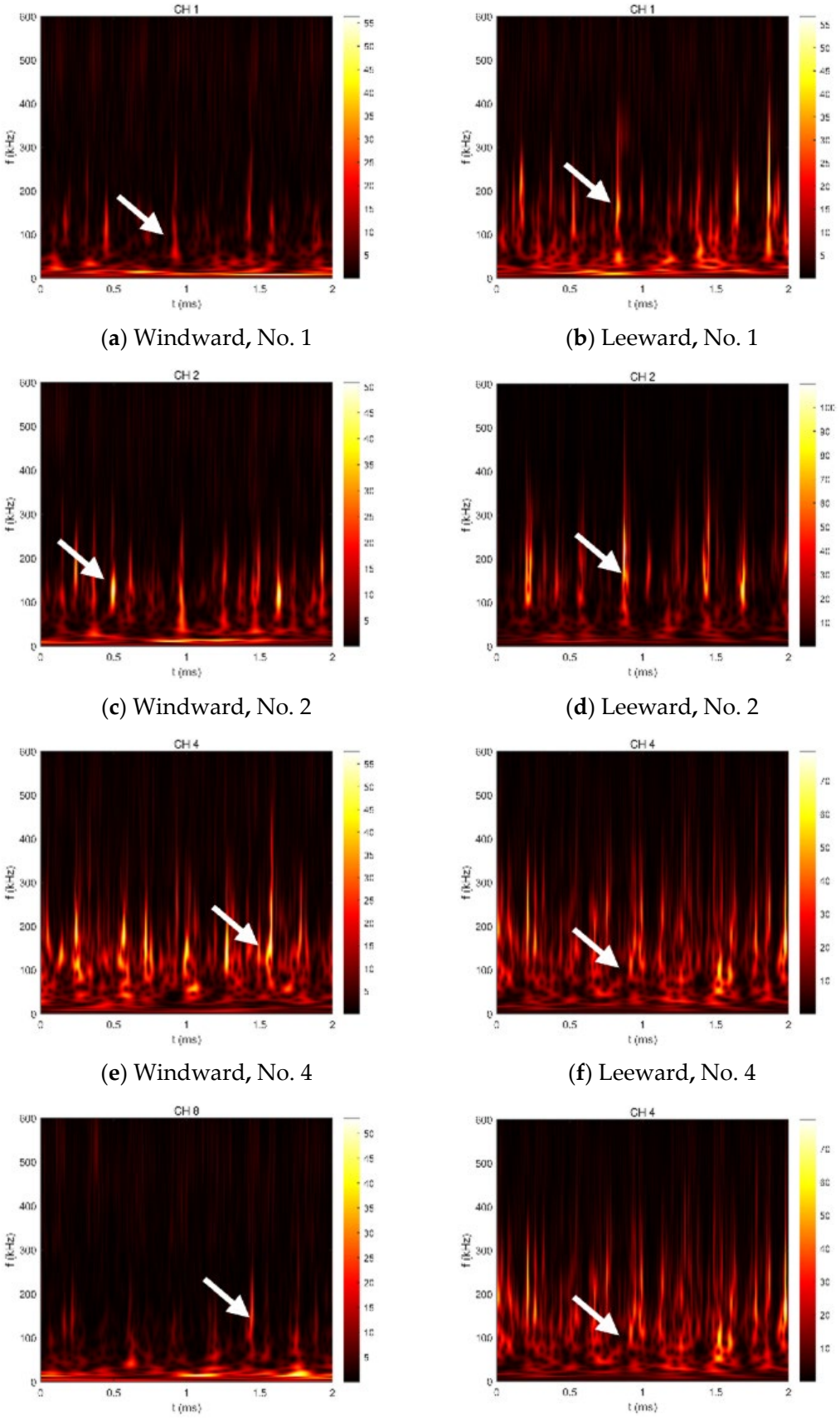


(**a**) Windward, PSD results (**b**) Leeward, PSD results

(**c**) Windward, Cross-correlation results (**d**) Leeward, Cross-correlation results

Figure 14. Power spectral density spectra and multi-sensor cross-correlation results of surface-pressure fluctuations in the fin surface regions R5 and R6.

The dominance of a crossflow-type mode on the fin surfaces can be attributed to the swept leading edge, which induces a spanwise pressure gradient over the fin. This spanwise pressure gradient drives a crossflow component within the boundary layer and produces an inflectional crossflow-velocity profile, which promotes crossflow instability growth. Also allows for a direct comparison between Regions R5 and R6. Both sides exhibit a low-frequency wave (70–180 kHz) characterized by intermittent high-energy streaks. The wave strengthens downstream and shows slight spectral broadening, consistent with wave packet growth and saturation. In Region R6, the same wave has slightly higher energy at mid-to-downstream stations and is more concentrated in time. Overall, Regions R5 and R6 show highly similar time–frequency behavior. The dominant instability in both regions is a low-frequency, crossflow-type mode. The remaining differences in energy levels are likely caused by mild asymmetry in geometry rather than a different instability mechanism.



(**a**) Windward, No. 1 (**b**) Leeward, No. 1

(**c**) Windward, No. 2 (**d**) Leeward, No. 2

(**e**) Windward, No. 4 (**f**) Leeward, No. 4

(**g**) Windward, No. 8 (**h**) Leeward, No. 8

Figure 15. Wavelet spectra of the surface-pressure signals at selected streamwise stations along the same streamline in the fin surface regions R5 and R6.

4. Conclusions

This study examines boundary layer stability on a hypersonic, asymmetric fin–cone-integrated configuration with a single swept fin at Mach 6 and 0° angle of attack. It focuses on how three-dimensional geometric features affect instability development and transition behavior at different surface locations. The main conclusions are summarized below.

The finless side shows a clear difference between the windward and leeward surfaces. In Region R1, a wave with peak frequency near 250 kHz strengthens downstream and convects at about $0.76U_e$. Rayleigh scattering images show coherent wave packets with a consistent convection speed. The results support the presence of high-frequency secondary instability during the nonlinear stage of a traveling crossflow mode. In Region R2, disturbances with the 140 to 280 kHz range amplify downstream and approach saturation. The convection speed is about $0.81U_e$. This behavior is consistent with Mack second-mode instability. Compared with the finless side, the fin–cone junction regions show more complex instability dynamics. In Region R3, the dominant wave is concentrated within 80 to 200 kHz and convects at about $0.89U_e$. Wavelet spectra indicate that the lower-frequency branch grows first and then enhances the higher-frequency content. Bicoherence indicates clear interactions within the high-frequency range. In Region R4, two bands appear at 60 to 120 kHz and 180 to 260 kHz. Bicoherence indicates strong high-frequency interactions and clear low-frequency to high-frequency interactions. The junction flow and the expansion-corner vortex system strongly modulate the instability spectrum. On the fin surfaces, the dominant behavior becomes more consistent on the windward and leeward sides. The fin surface regions are dominated by a crossflow-type mode. Wavelet spectra show intermittent wave packets in 70 to 180 kHz on both the windward and leeward fin surfaces. Differences are mainly in energy level and saturation location. Higher-frequency components remain sparse and are linked to the nonlinear development of the primary mode. In future work, particular focus will be placed on the high-resolution measurements of the fin–cone junction region and investigations into multi-mode coupling mechanisms, aiming to provide further insights into the boundary layer instability details of the blended-wing-body configuration.

A comprehensive analysis of the experimental results indicates that the fin–cone junction strongly modulates instability development and alters both the dominant mechanisms and the transition location. Future work will conduct higher-resolution measurements, like the hot wire technique in the junction region, and examine multi-mode coupling to further clarify boundary layer instability in fin–cone integrated configurations.

Author Contributions: Conceptualization, J.W.; methodology, D.L.; formal analysis, D.L.; investigation, F.Z.; resources, J.W.; data curation, Y.Y. and X.L.; validation, Y.Y. and X.L.; writing—original draft preparation, D.L.; writing—review and editing, J.W. and X.L.; visualization, D.L.; supervision, F.Z. and J.W.; project administration, F.Z.; funding acquisition, J.W. All authors have read and agreed to the published version of the manuscript.

Funding: This research received no external funding.

Data Availability Statement: The data presented in this study are available on request from the corresponding author.

Conflicts of Interest: The authors declare no conflicts of interest.

Abbreviations

The following abbreviations are used in this manuscript:

TSP	Temperature-Sensitive Paint
PCB	Piezotronics Inc., USA
PEEK	Polyether ether ketone

IR	Infrared thermography
PSD	Power spectral density
SBLI	Shock/Boundary Layer Interaction
R1	Windward Finless Region
R2	Leeward Finless Region
R3	Windward Fin–Cone Junction Region
R4	Leeward Fin–Cone Junction Region
R5	Windward Fin Surface Region
R6	Leeward Fin Surface Region

References

1. Fedorov, A. Transition and Stability of High-Speed Boundary Layers. *Annu. Rev. Fluid Mech.* **2011**, *43*, 79–95. [CrossRef]
2. Lee, C.; Chen, S. Recent Progress in the Study of Transition in the Hypersonic Boundary Layer. *Natl. Sci. Rev.* **2019**, *6*, 155–170. [CrossRef] [PubMed]
3. Zhao, R.; Wen, C.; Zhou, Y.; Tu, G.; Lei, J. Review of Acoustic Metasurfaces for Hypersonic Boundary Layer Stabilization. *Prog. Aerosp. Sci.* **2022**, *130*, 100808. [CrossRef]
4. Anderson, J.D. *Hypersonic and High-Temperature Gas Dynamics*, 3rd ed.; American Institute of Aeronautics and Astronautics, Inc.: Reston, VA, USA, 2019; ISBN 978-1-62410-514-2.
5. Yang, H.; Liang, H.; Zhang, C.; Wu, Y.; Zong, H.; Su, Z.; Kong, Y.; Zhang, D.; Li, Y. Investigation of Hypersonic Cone Boundary Layer Stability Regulation with Plasma Actuation. *Phys. Fluids* **2023**, *35*, 024112. [CrossRef]
6. Chen, L.; Guo, Q.; Qin, L.; Zhang, H. Hypersonic Shock Wave/Boundary Layer Interactions by a Third-Order Optimized Symmetric WENO Scheme. *Trans. Nanjing Univ. Aeronaut. Astronaut.* **2017**, *34*, 524–534.
7. Paredes, P.; Choudhari, M.M.; Li, F. Mechanism for Frustum Transition over Blunt Cones at Hypersonic Speeds. *J. Fluid Mech.* **2020**, *894*, A22. [CrossRef]
8. Murphy, K.J.; Nowak, R.J.; Thompson, R.A.; Hollis, B.R.; Prabhu, R.K. X-33 Hypersonic Aerodynamic Characteristics. In Proceedings of the AIAA Atmospheric Flight Mechanics Conference and Exhibit, Portland, OR, USA, 9–11 August 1999.
9. Hank, J.M.; Murphy, J.S.; Mutzman, R.C. The X-51A Scramjet Engine Flight Demonstration Program. In Proceedings of the 15th AIAA International Space Planes and Hypersonic Systems and Technologies Conference, Dayton, OH, USA, 28 April–1 May 2008; AIAA Paper 2008-2540.
10. Borg, M.P.; Schneider, S.P.; Juliano, T.J. Effect of Freestream Noise on Roughness-Induced Transition for the X-51A Forebody. In Proceedings of the 46th AIAA Aerospace Sciences Meeting and Exhibit, Reno, NV, USA, 9 January 2008; AIAA Paper 2008-0592.
11. Juliano, T.J.; Borg, M.P.; Schneider, S.P. Quiet Tunnel Measurements of HIFiRE-5 Boundary-Layer Transition. *AIAA J.* **2015**, *53*, 832–846. [CrossRef]
12. Juliano, T.J.; Adamczak, D.; Kimmel, R.L. HIFiRE-5 Flight Test Results. *J. Spacecr. Rocket.* **2015**, *52*, 650–663. [CrossRef]
13. Johnston, Z.M.; Candler, G.V. Hypersonic Simulations of the BoLT-II Subscale Geometry. In *Proceedings of the AIAA Scitech 2021 Forum, Virtual Event, 11 January 2021*; American Institute of Aeronautics and Astronautics: Reston, VA, USA, 2021.
14. Butler, C.; McKiernan, G.; Wheaton, B.M. Initial BiGlobal Stability Analysis of the BOLT II Flight Experiment. In *Proceedings of the AIAA SCITECH 2023 Forum, National Harbor, MD, USA, 23 January 2023*; American Institute of Aeronautics and Astronautics: Reston, VA, USA, 2023.
15. Zhang, C.; Lyu, D.; Zhu, C.; Chen, J.; Wu, J. Preliminary Experimental Study on Hypersonic Boundary Layer Stability of HyTRV Lift Body. *Acta Aeronaut. Astronaut. Sin.* **2025**, *46*, 130272.
16. Zhang, L.; Chen, X.; Liu, S.; Wang, Q.; Dong, S.; Duan, M.; Chen, J. Transition Front Prediction for the HyTRV Model Based on Multi-Dimensional Stability Theories. *Adv. Aerodyn.* **2025**, *7*, 9. [CrossRef]
17. Gillerlain, J., Jr. Fin-Cone Interference Flow Field. In *Proceedings of the 17th Aerospace Sciences Meeting, New Orleans, LA, USA, 15 January 1979*; American Institute of Aeronautics and Astronautics: Reston, VA, USA, 1979.
18. Mullen, C.D.; Turbeville, F.D.; Reed, H.L.; Schneider, S.P. Computational and Experimental Boundary-Layer Stability Analysis on a Hypersonic Finned Cone. In *Proceedings of the AIAA Scitech 2019 Forum, San Diego, CA, USA, 7 January 2019*; American Institute of Aeronautics and Astronautics: Reston, VA, USA.
19. Turbeville, F.D.; Schneider, S.P. Boundary-Layer Instability on a Slender Cone with Highly Swept Fins. In *Proceedings of the 2018 Fluid Dynamics Conference, Atlanta, GA, USA, 25 June 2018*; American Institute of Aeronautics and Astronautics: Reston, VA, USA, 2018.
20. Turbeville, F.D.; Schneider, S.P. Effect of Nose Bluntness on Fin-Cone Transition at Mach 6. In *Proceedings of the AIAA AVIATION 2021 Forum, Virtual Event, 2 August 2021*; American Institute of Aeronautics and Astronautics: Reston, VA, USA, 2021.

21. Turbeville, F.D.; Schneider, S.P. Effect of Freestream Noise on Fin-Cone Transition at Mach 6. In *Proceedings of the AIAA AVIATION 2022 Forum, Chicago, IL, USA, 27 June 2022*; American Institute of Aeronautics and Astronautics: Reston, VA, USA, 2022.
22. Knutson, A.; Gs, S.; Candler, G.V. Direct Numerical Simulation of Mach 6 Flow over a Cone with a Highly Swept Fin. In *Proceedings of the 2018 AIAA Aerospace Sciences Meeting, Kissimmee, FL, USA, 8 January 2018*; American Institute of Aeronautics and Astronautics: Reston, VA, USA, 2018.
23. Knutson, A.; Gs, S.; Candler, G.V. Instabilities in Mach 6 Flow over a Cone with a Swept Fin. In *Proceedings of the 2018 Fluid Dynamics Conference, Atlanta, GA, USA, 25 June 2018*; American Institute of Aeronautics and Astronautics: Reston, VA, USA, 2018.
24. Turbeville, F.D.; Schneider, S.P. Measurements of Instability and Transition on a Slender Cone with a Highly-Swept Fin at Mach 6. In *Proceedings of the AIAA SCITECH 2022 Forum, San Diego, CA, USA, 3 January 2022*; American Institute of Aeronautics and Astronautics: Reston, VA, USA, 2022.
25. Turbeville, F.D.; Schneider, S.P. Transition on a Cone with a Highly-Swept Fin at Mach 6. In *Proceedings of the AIAA Aviation 2019 Forum, Dallas, TX, USA, 17 June 2019*; American Institute of Aeronautics and Astronautics: Reston, VA, USA, 2019.
26. McMillan, M.; Mullen, C.D.; Reed, H.L. Spatial BiGlobal Stability Analysis of Spanwise Vortex Rollup on a Hypersonic Finned Cone. In *Proceedings of the AIAA AVIATION 2021 Forum, Virtual Event, 2 August 2021*; American Institute of Aeronautics and Astronautics: Reston, VA, USA, 2021.
27. Riha, A.K.; McMillan, M.; Reed, H.L. Linear Stability of a Boundary-Layer Vortex on a Hypersonic Finned Cone. In *Proceedings of the AIAA AVIATION 2021 Forum, Virtual Event, 2 August 2021*; American Institute of Aeronautics and Astronautics: Reston, VA, USA, 2021.
28. Middlebrooks, J.B.; Corke, T.C.; Matlis, E.; Semper, M. Cross-Flow Instability on a Swept-Fin Cone at Mach 6: Characteristics and Control. *J. Fluid Mech.* **2024**, *981*, A18. [CrossRef]
29. Middlebrooks, J.B.; Farnan, E.; Matlis, E.H.; Corke, T.C.; Mullen, C.D.; Peck, M.M.; Reed, H.L. Design of a Hypersonic Boundary Layer Transition Control Experiment Utilizing a Swept Fin Cone Geometry in Mach 6 Flow. In *Proceedings of the AIAA Scitech 2021 Forum, Virtual Event, 11 January 2021*; American Institute of Aeronautics and Astronautics: Reston, VA, USA, 2021.
30. Middlebrooks, J.B.; Farnan, E.; Juliano, T.J.; Matlis, E.H.; Corke, T.C.; Peck, M.M.; Mullen, D.; Reed, H.L.; Semper, M. Cross-Flow Instability Experiments on a Swept Fin-Cone with Variable Nose Bluntness in Mach 6 Flow. In *Proceedings of the AIAA SCITECH 2022 Forum, San Diego, CA, USA, 3 January 2022*; American Institute of Aeronautics and Astronautics: Reston, VA, USA, 2022.
31. Peck, M.M.; Groot, K.J.; Reed, H.L. Boundary-Layer Instability on a Highly Swept Fin on a Cone at Mach 6. *J. Fluid Mech.* **2024**, *987*, A13. [CrossRef]
32. Peck, M.M.; Groot, K.J.; Reed, H.L. Boundary-Layer Instability on a Highly Swept Fin on a Hypersonic Cone. In *Proceedings of the AIAA AVIATION 2022 Forum, Chicago, IL, USA, 27 June 2022*; American Institute of Aeronautics and Astronautics: Reston, VA, USA, 2022.
33. Meng, Q.; Lei, J.; Wu, S.; Yuan, C.; Yu, J.; Zhou, L. High Reynolds and Mach Number Effects on Transition Behavior on a Flared Cone–Swept Fin Configuration. *Phys. Fluids* **2025**, *37*, 064106. [CrossRef]
34. Meng, Q.; Lei, J.; Wu, S.; Yuan, C.; Yu, J.; Zhou, L. Angle of Attack Effects on Boundary Layer Transition over a Flared Cone–Swept Fin Configuration. *Aerospace* **2025**, *12*, 824. [CrossRef]
35. Li, X.; Xu, B.; Huang, G.; Wu, J. Experimental Study on the Boundary Layer Transition of a High-Speed Fin-Cone Configuration. *Adv. Aerodyn.* **2025**, *7*, 10. [CrossRef]
36. Huang, R.; Zhang, C.; Li, C.; Xu, B.; Xu, D.; Yuan, X.; Wu, J. Design and Preliminary Freestream Calibration of HUST Φ 0.5 m Mach 6 Ludwieg Tube Wind Tunnel. *Acta Aerodyn. Sin.* **2023**, *41*, 39–48, 85.
37. Li, X.; Li, C.; Wei, S.; Wu, J. Experiment of influence of distributed roughness elements on hypersonic boundary layer instability. *Acta Aeronaut. Astronaut. Sin.* **2024**, *45*, 90–108.
38. Qiu, H.; Shi, M.; Zhu, Y.; Lee, C. Boundary Layer Transition of Hypersonic Flow over a Delta Wing. *J. Fluid Mech.* **2024**, *980*, A57. [CrossRef]
39. Niu, H.; Yi, S.; Liu, X.; Huo, J.; Jin, L. Experimental Investigation of Nose-Tip Bluntness Effects on the Hypersonic Crossflow Instability over a Cone. *Int. J. Heat Fluid Flow* **2020**, *86*, 108746. [CrossRef]

Disclaimer/Publisher's Note: The statements, opinions and data contained in all publications are solely those of the individual author(s) and contributor(s) and not of MDPI and/or the editor(s). MDPI and/or the editor(s) disclaim responsibility for any injury to people or property resulting from any ideas, methods, instructions or products referred to in the content.